1996

CHARACTERIZING THE DYNAMIC RESPONSE OF A THERMALLY LOADED, ACOUSTICALLY EXCITED PLATE

K. D. Murphy
University of Nebraska-Lincoln

L. N. Virgin
Duke University

S. A. Rizzi
NASA Langley Research Center

Journal of Sound and Vibration (1996) **196**(5), 635–658

CHARACTERIZING THE DYNAMIC RESPONSE OF A THERMALLY LOADED, ACOUSTICALLY EXCITED PLATE

K. D. MURPHY

Department of Engineering Mechanics, University of Nebraska, Lincoln, NE 68588-0347, *U.S.A.*

L. N. VIRGIN

Department of Mechanical Engineering, Duke University, Durham, NC 27708-0300, *U.S.A.*

AND

S. A. RIZZI

NASA Langley Research Center, Structural Acoustics Branch, Hampton, VA 23681-0001, *U.S.A.*

(*Received* 14 *June* 1995, *and in final form* 26 *February* 1996)

In this work the dynamic response is considered of a homogeneous, fully clamped rectangular plate subject to spatially uniform thermal loads and narrow-band acoustic excitation. In both the pre- and post-buckled regimes, the small amplitude, linear response is confirmed. However, the primary focus is on the large amplitude, non-linear, snap-through response, because of the obvious implications for fatigue in aircraft components.

A theoretical model is developed which uses nine spatial modes and incorporates initial imperfections and non-ideal boundary conditions. Because of the higher order nature of this model, it is inherently more complicated than a one-mode buckled beam equation (Duffing's equation). An experimental system was developed to complement the theoretical results, and also to measure certain system parameters for the model which are not available theoretically.

Several analysis techniques are used to characterize the response. These include time series, power spectra and autocorrelation functions. In addition, the fractal dimension and Lyapunov exponents for the response are computed to address the issue of spatial dimension and temporal complexity (chaos), respectively. Comparisons between theory and experiment are made and show considerable agreement. However, these comparisons also serve to point out difficulties in computing the fractal dimension and Lyapunov exponents from experimental data.

1. INTRODUCTION

Structural vibrations caused by intense acoustic excitation are common in aircraft and spacecraft. Combined with the elevated temperatures, typical steady-state oscillations may consist of small amplitude motions about one equilibrium or large amplitude, snap-through motions about and between multiple equilibria. In either case, structural fatigue may result and severely reduce the life of the structure [1, 2].

Previous studies in snap-through dynamics have looked at a variety of excitations including aerodynamic [3, 4], acoustic [5, 6], harmonic [7] and stochastic [8]. While some

0022–460X/96/400635 + 24 $18.00/0

include experiments, these studies have typically focused on modelling the system and viewing the response in the time and frequency domains.

The goal of this research endeavor is to demonstrate and characterize some typical behavior of an acoustically excited and thermally loaded plate. Specifically, the response is seen in terms of time series, phase plane projections, power spectra and autocorrelation functions. In the case of periodic oscillations, these techniques are sufficient. However, for snap-through motions, these methods provide only qualitative answers which suggest that the motion is complex. Therefore, other quantities such as the fractal dimension and Lyapunov exponents are used to quantify the "size" of the system and the temporal complexity of the response, respectively.

2. EXPERIMENTAL FACILITIES

The experiments were conducted in the Thermal Acoustic Fatigue Apparatus (TAFA) at the NASA Langley Research Center [9]. TAFA is a progressive wave tube facility used to test plate structures under acoustic, thermal or combined loads. A schematic top view of TAFA is shown in Figure 1.

Acoustic excitation is provided by a set of air modulators connected through an exponential horn to a 6 ft $\times$ 6 ft $\times$ 1 ft test section which leads to an anechoic termination. Test specimens are mounted on the side wall of the test section and are therefore subjected to a grazing acoustic load. This system is capable of generating overall sound pressure levels between 125 dB and 165 dB. Excitation frequencies may be either sinusoidal or broadband in the range of 40–500 Hz.

Radiant thermal loads are generated by a set of ten quartz lamp banks situated directly across the test section from the plate. The lamps are controlled in either a percentage power or a temperature set point mode. A low mass airflow is also used to minimize the effects of natural convection, thereby producing a more uniform temperature distribution across the plate.

The clamping frame was designed specifically for high temperature applications. The design minimizes thermal expansion of the frame during heating such that in-plane compression of the plate results. A detailed description of this system is provided in reference [10].

Data were acquired using high temperature strain gages at $(x/a, y/b) = (0{\cdot}583, 0{\cdot}461)$, which measured the y-direction strain (perpendicular to the direction of the acoustic wave propagation). This location was chosen because it does not coincide with any nodal lines in the lower modes. Strain gage data was recorded using a workstation based acquisition system with a sampling rate of 32 768 samples/s. Measurements were DC coupled in order to record the strains at the various equilibrium positions. The plate was also outfitted with

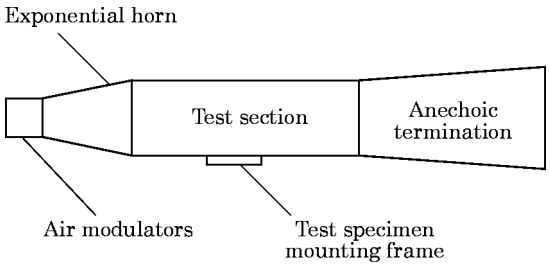

Figure 1. A schematic top view of the Thermal Acoustic Fatigue Apparatus (TAFA) at the NASA Langley Research Center.

several thermocouples to monitor the temperature and to verify that a relatively uniform distribution was created.

The plate under consideration has dimensions $15\text{ in} \times 12\text{ in} \times 0{\cdot}062\text{ in}$ (aspect ratio $= a/b = 1{\cdot}25$) and was made of AISI 321 stainless steel. The material properties of this steel are as follows: $E = 28 \times 10^6$ psi, $\nu = 0{\cdot}33$, $\alpha = 9{\cdot}6 \times 10^{-6}$ (in/in)/°F and $\rho = 0{\cdot}29\text{ lb/in}^3$. Using the techniques described in reference [10], the critical temperature rise above ambient for the flat plate (i.e., the buckling temperature) with experimental boundary conditions was found to be $\Delta T_{cr}^{flat} = 21°\text{F}$.

3. THEORETICAL MODEL

3.1. GOVERNING EQUATIONS

The non-linear partial differential equation of motion for this sytem is given by

$$\acute{V}^4 w - \left(\frac{a}{b}\right)^2\left[\frac{\partial^2 F}{\partial \eta^2}\left(\frac{\partial^2 w}{\partial \xi^2} + \frac{\partial^2 w_0}{\partial \xi^2}\right) + \frac{\partial^2 F}{\partial \xi^2}\left(\frac{\partial^2 w}{\partial \eta^2} + \frac{\partial^2 w_0}{\partial \eta^2}\right)\right.$$

$$\left. - 2\,\frac{\partial^2 F}{\partial \xi\,\partial \eta}\left(\frac{\partial^2 w}{\partial \xi\,\partial \eta} + \frac{\partial^2 w_0}{\partial \xi\,\partial \eta}\right)\right] + \frac{\partial^2 w}{\partial \tau^2} + \beta\,\frac{\partial w}{\partial \tau} + \Delta P = 0, \tag{1}$$

where w is the lateral displacement of the plate, w_0 is the initial imperfection, ΔP is an external load and F is the Airy stress function. Thermal effects are included in the Airy stress function [10]. In addition, ξ and η are non-dimensional spatial co-ordinates, τ is a non-dimensional time and $\acute{V}^4$ is a non-dimensional biharmonic operator, these being given by

$$\xi = \frac{x}{a}, \qquad \eta = \frac{y}{b}, \qquad \tau = t\sqrt{\frac{D}{\rho h a^4}},$$

$$\acute{V}^4 = \left(\frac{1}{a^4}\right)\left[\frac{\partial^4}{\partial \xi^4} + 2\left(\frac{a}{b}\right)^2 \frac{\partial^4}{\partial \xi^2\,\partial \eta^2} + \left(\frac{a}{b}\right)^4 \frac{\partial^4}{\partial \eta^4}\right],$$

where a and b are the lengths of the plate in the x- and y-directions, h is the plate thickness, D is the flexural rigidity and ρ is the material density.

Compatibility between the in-plane stress and the lateral displacement, w, is assured by satisfying

$$\acute{V}^4 F = 12(1 - \nu^2)\left(\frac{a}{b}\right)^2\left[\left(\frac{\partial^2 w}{\partial \xi\,\partial \eta}\right)^2 + 2\left(\frac{\partial^2 w}{\partial \xi\,\partial \eta}\right)\left(\frac{\partial^2 w_0}{\partial \xi\,\partial \eta}\right)\right.$$

$$\left. - \frac{\partial^2 w}{\partial \xi^2}\frac{\partial^2 w}{\partial \eta^2} - \frac{\partial^2 w}{\partial \xi^2}\frac{\partial^2 w_0}{\partial \eta^2} - \frac{\partial^2 w}{\partial \eta^2}\frac{\partial^2 w_0}{\partial \xi^2}\right], \tag{2}$$

where ν is the Poisson ratio. A derivation and discussion of these equations are available in references [11–13].

3.2. SOLUTION PROCEDURE

The solution procedure, outlined here, is described in detail in reference [10]. This procedure assumes an out-of-plane displacement field, w, and an initial geometric imperfection, w_0, of the form

$$w(\xi, \eta, \tau) = \sum_{i=1}^{3} \sum_{j=1}^{3} a_{ij}(\tau) \Psi_i(\xi) \Phi_j(\eta), \qquad w_0(\xi, \eta) = \tilde{a}_{mn} \tilde{\Psi}_m(\xi) \tilde{\Phi}_n(\eta). \tag{3}$$

The modal coefficients, $a_{ij}(\tau)$, are the time dependent generalized co-ordinates. These co-ordinates, along with their velocity counterparts $\dot{a}_{ij}$, make up the state variables. Since three spatial modes are assumed in each direction, there are nine a_{ij}'s and 18 state variables. The comparison functions Ψ_i and Φ_j are the cosine functions presented in reference [14]:

$$\Psi_i(\xi) = \cos([i-1]\pi\xi) - \cos([i+1]\pi\xi), \qquad \Phi_j(\eta) = \cos([j-1]\pi\eta) - \cos([j+1]\pi\eta). \tag{4}$$

The tilde ($\tilde{}$) notation is used to indicate which terms are related to the initial imperfection.

First, the compatibility equation is considered. By substituting equation (3) into the right side of equation (2), it becomes evident that the particular solution to the Airy stress function, F_p, must take the form

$$F_p(\xi, \eta, \tau) = \sum_i \sum_j \sum_k \sum_l a_{ij}(\tau) a_{kl}(\tau) F^{I}_{ijkl}(\xi, \eta) + \sum_i \sum_j a_{ij}(\tau) \tilde{a}_{mn} F^{II}_{ij}(\xi, \eta). \tag{5}$$

Expanding the spatial terms F^{I}_{ijkl} and F^{II}_{ij} in the assumed mode shapes with constant coefficients $\mathscr{F}^{I}_{pqijkl}$ and $\mathscr{F}^{II}_{pqij}$ gives two spatial equations:

$$\sum_p \sum_q \mathscr{F}^{I}_{pqijkl} (\acute{\nabla}^4 \Psi_p \Phi_q) = 12(1-\nu^2) \left(\frac{a}{b}\right)^2 [\Psi_i' \Phi_j' \Psi_k' \Phi_l' - \Psi_i'' \Phi_j \Psi_k \Phi_l''], \tag{6}$$

$$\sum_p \sum_q \mathscr{F}^{II}_{pqij} (\acute{\nabla}^4 \Psi_p \Phi_q) = 12(1-\nu^2) \left(\frac{a}{b}\right)^2 [2\Psi_i' \Phi_j' \tilde{\Psi}_m' \tilde{\Phi}_n' - \Psi_i'' \Phi_j \tilde{\Psi}_m \tilde{\Phi}_n'' - \Psi_i \Phi_j'' \tilde{\Psi}_m'' \tilde{\Phi}_n]. \tag{7}$$

Galerkin's method is then applied and, from the resulting algebraic equations, the coefficients $\mathscr{F}^{I}_{pqijkl}$ and F^{II}_{pqij} may be obtained numerically.

The particular solution, F_p, only contributes inside the domain, since it is expanded in terms of the assumed modes ($\Psi_i = \Phi_i = 0$ on the boundaries). Therefore, the homogeneous solution, F_h, must account for the edge stress. An appropriate homogeneous solution is

$$F_h = \tfrac{1}{2}(\bar{N}_\xi \eta^2 + \bar{N}_\eta \xi^2), \tag{8}$$

where $\bar{N}_\xi$ and $\bar{N}_\eta$ are the in-plane edge stresses. These terms may be obtained by enforcing a combined stress–displacement boundary condition. The stress is made proportional to the average in-plane displacements:

$$\bar{N}_\xi = -\left(\frac{a}{h}\right) K_\xi \int_0^1 \Delta_\xi \, \mathrm{d}\eta, \qquad \bar{N}_\eta = -\left(\frac{b}{h}\right) K_\eta \int_0^1 \Delta_\eta \, \mathrm{d}\xi, \tag{9}$$

where K_ξ and K_η are the equivalent in-plane boundary stiffnesses and $\Delta_\xi = u(1, \eta) - u(0, \eta)$ and $\Delta_\eta = v(\xi, 1) - v(\xi, 0)$ represent the in-plane stretching. Expressions for the x and y

in-plane displacements, u and v, come from combining the non-linear stress–strain and strain–displacement relations and integrating: $u = \int_0^1 (\partial u/\partial \xi)\, \mathrm{d}\xi$ and $v = \int_0^1 (\partial v/\partial \eta)\, \mathrm{d}\eta$.

Finally, the Airy stress function, $F = F_p + F_h$, and the displacement field (equation (3)) are then substituted into equation (1) and Galerkin's procedure is carried out. This leaves $r \times s$ non-linear, coupled ODE's in the modal coefficients, a_{ij}. The rsth equation takes the form

$$\sum_i \sum_j S_{ijrs}\ddot{a}_{ij} + \sum_i \sum_j \beta_{ijrs} S_{ijrs}\dot{a}_{ij} + \sum_i \sum_j \sum_k \sum_l \sum_p \sum_q B_{ijklpqrs} a_{ij} a_{kl} a_{pq}$$

$$+ \sum_i \sum_j \sum_k \sum_l C_{ijklrs} a_{ij} a_{kl} + \sum_i \sum_j D_{ijrs} a_{ij} + E_{rs} = \Delta P_{rs}, \tag{10}$$

where S_{ijrs} are modal mass terms, β_{ijrs} are proportional damping coefficients and ΔP_{rs} are excitation terms. The other coefficients, $B_{ijklpqrs}$, C_{ijklrs}, D_{ijrs} and E_{rs}, are stiffness related. Due to the cubic nature of the stiffness, these non-linear ODE's may be seen as a set of higher order, coupled Duffing's equations.

It should be noted that three obstacles prevent the immediate use of this model. The first two are the initial geometric imperfection (deflection), $\tilde{a}_{mn}$ and the in-plane boundary stiffnesses, K_ξ and K_η. Appropriate values were obtained using Southwell's technique as described in references [10] and [15]. For the 0·062 in plate, the non-dimensional in-plane boundary stiffness is $K_\xi = K_\eta = 2050$ and the initial imperfection was $\tilde{a}_{11} = 0{\cdot}04$. The third obstacle is the structural damping. The procedure to measure the damping is described in the following section.

3.3. STRUCTURAL DAMPING

For simplicity, a linear viscous damping model is assumed. This simple model does capture the essential behavior of the system and, provided that the damping is measured experimentally, may be used in the structural model with a reasonable degree of confidence.

To estimate the damping ratio, the half-power method is used [16]: ζ_{11} is found by applying a narrow-band acoustic excitation near the first mode resonant frequency of the plate. Using the strain gage (output) and microphone (input) signals, the transfer function is computed. From the fundamental peak, the damping in the first mode is computed by

$$\zeta_{11} = \tfrac{1}{2}[(\omega_2 - \omega_1)/\omega_p], \tag{11}$$

where ω_p is the peak frequency and ω_1 and ω_2 are the frequencies at $1/\sqrt{2}$ of the peak. Based on this procedure, the damping ratio is estimated as $\zeta_{11} = 0{\cdot}01$.

The damping ratios in the other modes are more difficult to find using the half-power method, because the peaks in the transfer function at higher frequencies are less distinct. It is assumed that the remainder of the damping ratios scale with their resonant frequencies [17]:

$$\zeta_{ij} = \zeta_{11}(\omega_{11}/\omega_{ij}). \tag{12}$$

However, equation (10) uses damping coefficients rather than the damping ratios. In this case, the damping in the ijth mode of the rsth equation is

$$\beta_{ijrs} = 2\zeta_{ij}\omega_{ij} = 2\zeta_{11}\omega_{11}. \tag{13}$$

It should be noted that the resonant frequencies are temperature dependent [10]. However,

for simplicity, ω_{11} in equation (13) is taken at the ambient temperature. As a result, β_{ijrs} is constant.

3.4. ACOUSTIC MODELLING

The model is completed by considering ΔP_{rs}. This excitation term results from the acoustic field in TAFA and is obtained in a two-step procedure. First, the pressure on an infinitely rigid plate is found. However, the flexible plate "pushes back" on the fluid and the pressure field is augmented. The actual pressure field differs because of this structural–fluid coupling. Modelling this fluid–structural coupling constitutes the second part of the solution procedure.

For the infinitely rigid plate, the problem becomes one of duct acoustics. The pressure field in TAFA is governed by the linear wave equation

$$\nabla^2 p = \frac{1}{c^2}\frac{\partial^2 p}{\partial t^2}, \tag{14}$$

subject to the boundary conditions

$$q_y(x, 0, z, t) = 0, \quad q_y(x, L_y, z, t) = 0, \quad q_z(x, y, 0, t) = 0, \quad q_z(x, y, L_z, t) = 0, \tag{15}$$

where p is the pressure field, c is the speed of sound in the fluid (air), and q_y and q_z are the fluid displacements in the y- and z-directions, respectively. L_y and L_z are the width and height dimensions of the duct. Using these boundary conditions along with the momentum equation allows one to find a solution to the wave equation (see reference [18]):

$$p(x, y, z, t) = \sum_m \sum_n p_{mn} \cos(m\pi y/L_y) \cos(n\pi z/L_z)\, \mathrm{e}^{\mathrm{i}(\omega t - k_{mn} x)}, \tag{16}$$

where

$$k_{mn} = \sqrt{(\omega/c)^2 - (m\pi/L_y)^2 - (n\pi/L_z)^2}. \tag{17}$$

The x-direction boundary condition must be used to compute the coefficients p_{mn}. The fluid displacement at $x = 0$ is assumed to be periodic and, therefore, plane waves are created. This can be stated $q_x(0, y, z, t) = q_0\, \mathrm{e}^{\mathrm{i}\omega t}$. Combining this and equation (16) with the x-component of the momentum equation and evaluating at the $x = 0$ boundary gives

$$\frac{\partial q_x}{\partial t} = -\frac{1}{\rho}\frac{\partial p}{\partial x}, \qquad q_0 = \frac{1}{\omega\rho}\sum_m \sum_n k_{mn} p_{mn} \cos\left(\frac{m\pi y}{L_y}\right) \cos\left(\frac{n\pi z}{L_z}\right), \tag{18}$$

where ρ is the density of the fluid (air). Matching cosine terms on the right and left sides yields $m = n = 0$. Since this is the only solution, the pressure coefficients and wavenumbers are all zero except for p_{00} and k_{00}, which are

$$p_{00} = q_0 \rho\omega/k_{00}, \qquad k_{00} = \omega/c. \tag{19}$$

Combining these terms with equation (16) gives an expression for the entire pressure field in the duct:

$$p(x, t) = p_0 \sin\left(\omega t - \frac{\omega}{c} x\right), \tag{20}$$

where $p_0 = q_0 \rho c$. Equation (20) may be used to compute the pressure on an infinitely rigid plate.

Next, the problem of fluid–structural coupling must be considered. One approach is to compute the radiative impedance of the fluid for a given loading situation. The impedance is a complex quantity relating the pressure and velocity. The real part (resistance) is in-phase with the velocity and, hence, is damping-like. The imaginary part (reactance) is 90° out-of-phase with the velocity, making it mass-like in the low frequency, incompressible case. As a result, computing the fluid impedance is similar to finding the additional damping or mass which would have to be added to the structure in order to create an equivalent loading scenario.

For the sake of this analysis, the plate is replaced by an equivalent circular piston moving in the fluid. The word "equivalent" means that the piston area equals the area of the rectangular plate. For this system, the equivalent piston has a radius $r = 7{\cdot}5694$ in.

The excitation frequency used through this study is in the vicinity of 100 Hz. This corresponds to a wavelength of $\lambda = 11{\cdot}25$ ft (in air at 68°F). Also, the wavenumber is $K = 2\pi/\lambda = 0{\cdot}046542\ \text{in}^{-1}$.

Expressions for the radiative resistance and reactance of a baffled circular piston are well known [18] and are given in non-dimensional form by

$$R_1(\bar{\omega}) = 1 - \frac{2\mathrm{J}_1(\bar{\omega})}{\bar{\omega}} = \frac{\bar{\omega}^2}{2^2 1!2!} - \frac{\bar{\omega}^4}{2^4 2!3!} + \cdots,$$

$$X_1(\bar{\omega}) = \frac{4}{\pi}\left[\frac{\bar{\omega}}{3} - \frac{\bar{\omega}^3}{3^2 \cdot 5} + \frac{\bar{\omega}^5}{3^2 \cdot 5^2 \cdot 7} + \cdots\right], \tag{21}$$

where R_1 is the resistance, X_1 is the reactance, J_1 is a Bessel function and $\bar{\omega} = 2kr$ is the reduced frequency, with k as the wavenumber.

For the experimental system under consideration, the reduced frequency is $2kr = 0{\cdot}7046$. In this low reduced frequency region, $R_1(\bar{\omega})$ and $X_1(\bar{\omega})$ can roughly be approximated by the leading term in their series expansions. This means that the resistance is quadratic in the reduced frequency, while the reactance is linear.

Using the low frequency reactance, an equivalent mass for the fluid may be found. In dimensional form the reactance may be written as $X = \pi r^2 \rho c X_1$. Also, the low frequency mechanical reactance is given by ωm, with ω in rad/s. Combining these leads to

$$m\omega = 2(\pi r^2)(\rho c)X_1(2kr) = 2\pi r^2 \rho \frac{8r}{3\pi}. \tag{22}$$

The constants for air are $\rho = 1{\cdot}3587 \times 10^{-6}$ slugs/in^3, $c = 1125$ ft/s and $\omega = ck$. The additional factor of 2 is added because there is fluid on each side of the plate. From equation (22) the equivalent mass of the fluid is $m = 0{\cdot}003143$ slugs, while the mass of the plate is $m_{plate} = 0{\cdot}1$ slugs. The effective fluid mass is two orders of magnitude smaller than the mass of the plate (structural mass) and may be neglected without significantly affecting the results.

The equivalent fluid damping may be computed using the dimensional resistance $R = \pi r^2 \rho c R_1$. The equivalent mechanical resistance is the damping coefficient, C. Equating the low frequency (quadratic) fluid resistance to the equivalent mechanical resistance and including the same factor of 2 gives

$$C = 2(\pi r^2)(\rho c)R_1(2kr) = 2(\pi r^2)(\rho c)[\tfrac{1}{8}(2kr)^2]. \tag{23}$$

Using the fluid constants provided earlier, the equivalent damping is $C = 0{\cdot}4098$ slugs/s. In terms of the damping ratio, this becomes $\zeta = C/2m\omega_n = 0{\cdot}003$. This value is an order

of magnitude smaller than the structural damping. Therefore, the fluid damping may also be ignored in this acoustic regime.

The results of this section suggest that the coupling between the plate and the air has negligible effect on the pressure experienced by the plate. In this case, the uncoupled pressure field given by equation (20) is a sufficient model for this system.

3.5. NUMERICAL ISSUES

Throughout this analysis, a nine-mode expansion is assumed for the time-varying displacement field. More specifically, the model consists of three modes in both the ξ and η directions and a first mode initial imperfection. As a result, equation (10) represents one equation, the rsth equation, of $r \times s = 9$ equations. In first order form, these equations may be written

$$\dot{\mathbf{x}} = [A]^{-1}\mathbf{f}(\mathbf{x}). \tag{24}$$

The matrix $[A]$ is time independent and, therefore, only needs to be computed once. These are 18 coupled, first order non-linear ODE's which must be integrated simultaneously.

The integration of the equations of motion is accomplished with the routine LSODA from the ODEPACK library [19]. This particular integration routine was selected for a number of reasons. First, it uses an adaptive time step which greatly increases computational efficiency. Second, it was designed to detect and account for numerical stiffness in the equations. Stiffness occurs when there is a large disparity in the magnitudes of the eigenvalues of the local Jacobian matrix [20] and, in physical terms, suggests that there are both long and short time scales involved in the response. Stiff problems present difficulties for standard integration routines and usually result in unbounded solutions. Alternatively, stiff equation solvers tend to be slow, inefficient routines. LSODA seeks to make the best of both worlds. Under ordinary circumstances, Geer's method [21] is used to integrate the equations of motion. During the integration, the eigenvalues of the Jacobian are continuously monitored and, if the problem becomes stiff, the routine switches to a backward difference formula (BDF) which is designed to handle stiff problems. Once the stiffness is past, the routine switches back to Geer's method. The plate equations may or may not be stiff depending on what system parameters are being considered. Furthermore, *a priori* information regarding the time dependent behavior of the eigenvalues of the Jacobian is not typically available. Consequently, this particular routine provides an efficient and reliable way to integrate the plate equations regardless of stiffness.

4. STATIC CONSIDERATIONS

In the context of this paper, a critical state is one in which, for small perturbations of a control parameter, multiple equilibria emerge.

A schematic of the typical static behavior of heated plates is shown in Figure 2. The non-dimensional out-of-plane displacement is plotted against the temperature rise above ambient, ΔT. The initially flat plate remains flat as the applied temperature increases until it experiences a supercritical pitchfork bifurcation (it buckles) at the critical point A. Above this value of ΔT the flat plate has two stable, symmetric equilibria and is, therefore, termed post-critical (post-buckled).

The initially imperfect plate experiences a gradual deflection with increasing ΔT. Above point B, which is another critical state, a secondary stable equilibrium branch appears. This critical state corresponds to a saddle-node bifurcation for the secondary branch. Here, the

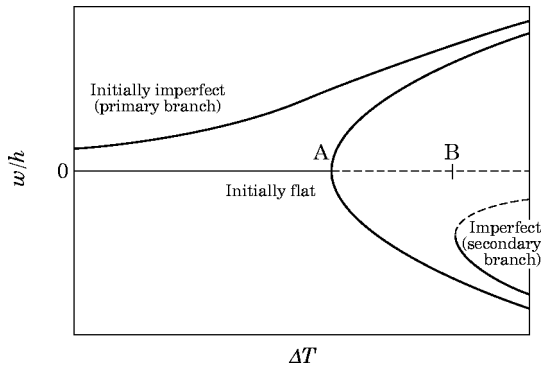

Figure 2. A static equilibrium diagram for the plate as a function of temperature rise above ambient. Both the initially flat and imperfect scenarios are shown.

equilibria are clearly unsymmetric and the presence of the imperfection actually postpones the onset of the critical state until a higher value of ΔT.

An actual plate would undoubtedly contain some initial curvature and would likely experience further deformation during clamping. Consequently, the static behavior of the system under consideration conforms more closely to the latter case.

It is worth noting that in a static sense the secondary branch corresponds to a very specific loading history. A typical loading scenario, which starts from the ambient ($\Delta T = 0$), would leave the system on the primary branch. Only by applying a large lateral load at a value of ΔT above point B would the system encounter the secondary branch. This type of lateral load, however, is entirely possible in the dynamic case.

This equilibrium diagram is useful because it underlies the possible dynamic responses of the system. In the pre-critical regime, both linear and non-linear responses are possible. Due to the unique equilibrium and the additional large amplitude membrane effects, any non-linear response would be of a hardening-spring type. In the post-critical regime, the situation is quite different. Again, both linear and non-linear responses may occur about either stable equilibrium but, in this case, the non-linear response would be of the softening-spring type because of the unstable equilibrium separating the two stable equilibria. Furthermore, in the post-critical regime, steady state snap-through oscillations are possible if the system experiences a sustained, high level excitation.

5. LOCAL BEHAVIOR

Small amplitude (local) oscillations constitute an important aspect of plate dynamics for a number of reasons. First, they are common at low excitation levels and at frequencies away from resonance. Hence, they are relevant from a practical point of view. Furthermore, the behavior of these oscillations may be viewed within the context of linear systems theory. As a result, these *linear* oscillations, while being important in their own right, serve as a necessary contrast for the large amplitude, non-linear behavior of the snap-through dynamics.

5.1. PRE-CRITICAL REGIME

To remain in the pre-critical regime, the system was heated to $\Delta T/\Delta T_{cr}^{flat} = \frac{1}{3}$. The excitation was set at a sound pressure level of 140 dB with $\omega = 63{\cdot}75$ Hz. This was well below the fundamental natural frequency of approximately 112 Hz.

The absolute displacement time history based on numerical simulation is shown in Figure 3(a). In Figure 3(c), the experimental counterpart is shown. However, in the latter case, the y-direction strain, ϵ_{yy}, is shown relative to the $\Delta T = 0$ clamped static equilibrium. Hence, an appreciable static offset is evident in the simulation but not in the experiment. Both oscillations appear periodic with a dominant period of roughly $T = 0{\cdot}0155$ s, which is very nearly the reciprocal of the forcing frequency.

An alternative approach to viewing the motion is to plot the velocity versus the displacement or, for the experiment, the strain against the time rate of change of strain. This idea comes from one-degree-of-freedom oscillators where x and $\dot{x}$ are the state variables and the $(x, \dot{x})$ plane is the phase plane. Because the plate is a continuous dynamical system with an infinite number of degrees of freedom, this type of plot as measured from one point on the structure does not constitute a true phase plane of the motion. Nonetheless, this pseudo-phase plane does give an indication of the complexity of the motion.

As in many mechanical systems, it is difficult experimentally to measure $\dot{\epsilon}_{yy}$. To avoid this problem, time delay embedding is used (see reference [22]). Instead of differentiating the strain to incorporate the effect of time, time delay embedding uses a phase lag. In other words, the response, $\epsilon_{yy}(t)$, is plotted against a time delayed version of itself, $\epsilon_{yy}(t + \tau)$. An appropriate time delay corresponds to the first zero crossing of the autocorrelation function as described in reference [23]. For this nearly linear response, the time delay turns out to be approximately one-quarter of the forcing period, $T/4$, as will be discussed shortly.

In Figures 3(b) and (d) are shown a pseudo-phase plane for the simulation and an embedded version based on the experiment, respectively. The static offset which is evident in the simulation does not appear in the experiment since the strain is measured relative to the equilibrium position. These nearly closed loop trajectories again suggest that the response is a period-one oscillation.

The motion may also be considered in the frequency domain. The power spectral densities (PSD's) for the responses are given in Figures 4(a) and (c). The numerical power spectra indicate the response is dominated by the peak at 64 Hz, while having small contributions at 125 Hz and 185 Hz. This agrees well with the experimental spectra in that

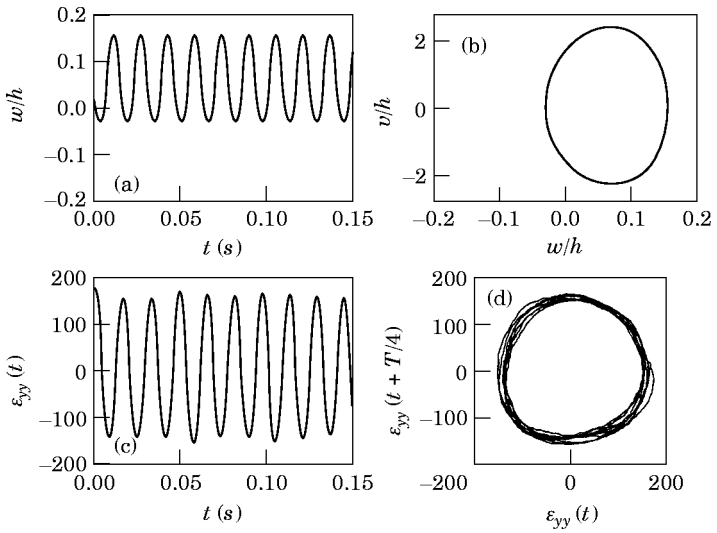

Figure 3. The unique, small amplitude response of the plate at $(\xi,\eta) = (0{\cdot}583,0{\cdot}416)$ with $\Delta T/\Delta T_{cr}^{flat} = 0{\cdot}333$, $\Delta P = 140$dB and $\omega = 63{\cdot}75$Hz; (a,b) numerical and (c,d) experimental.

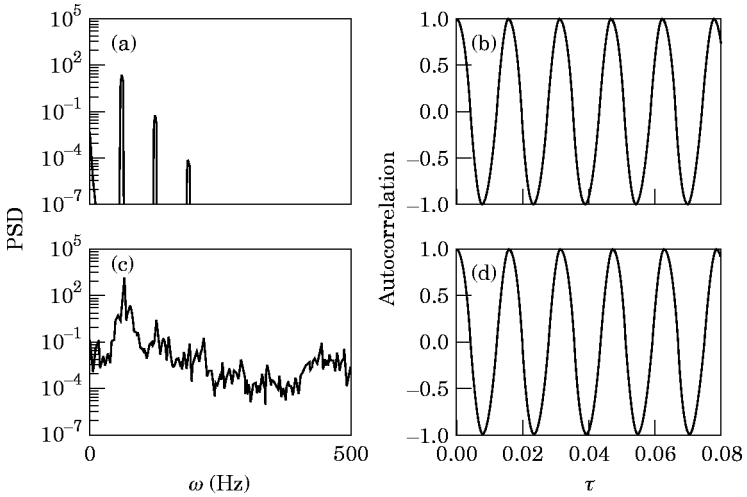

Figure 4. Numerical (a,b) and experimental (c,d) power spectra and correlation functions for the response in Figure 3.

the peaks occur at the same frequencies and are of similar amplitude. The experimental results also indicate a low level continuous distribution of energy throughout the frequency range, which can be attributed to the noise generation system in TAFA.

The temporal complexity of a response may also be measured using the autocorrelation function (see reference [24]). The autocorrelation function for the simulation, shown in Figure 4(b), confirms that the response is periodic; while the experiment (see Figure 4(d)) experiences a mild loss in correlation, indicating that the response is very nearly periodic. Both of these results suggest that the first zero crossing of the autocorrelation function is at about 0·004 s, or about a quarter of the forcing cycle. This characteristic time scale is used as an appropriate embedding delay in Figure 3(d) [23].

These results convey several important facts. First, at these parameter values, the agreement between the theoretical model and the experiment is good. This suggests that the non-linear model is capable, at the very least, of describing the small amplitude temporal behavior of the pre-critical plate. Also, the system response may be classified as linear (harmonic), in part, because the response is periodic and dominated by the excitation frequency. This assertion is further supported by the first zero crossing time of the autocorrelation function. The first zero crossing of a harmonic oscillation is exactly $T/4$, which is roughly the result found both numerically and experimentally.

5.2. POST-CRITICAL REGIME

To enter the post-critical regime, the system was heated to $\Delta T/\Delta T_{cr}^{flat} = 1{\cdot}762$. A harmonic acoustic excitation was provided at a sound pressure level of 130 dB and a frequency of $\omega = 120$ Hz, driving the plate at the experimentally measured fundamental frequency at this temperature.

The responses at these parameter values for the simulation (a, b) and the experiment (c, d) are shown in Figure 5. Each figure uses two sets of data to show the coexisting oscillations. Clearly, both of these oscillations are small amplitude events and are a considerable distance apart, suggesting that they reside in separate regions of the phase space. In both the simulation and experiment, the primary and secondary oscillations appear to be periodic. Also, these oscillations are not quite symmetric about the origin, which is in agreement with the mild asymmetry of the equilibrium branches in Figure 2.

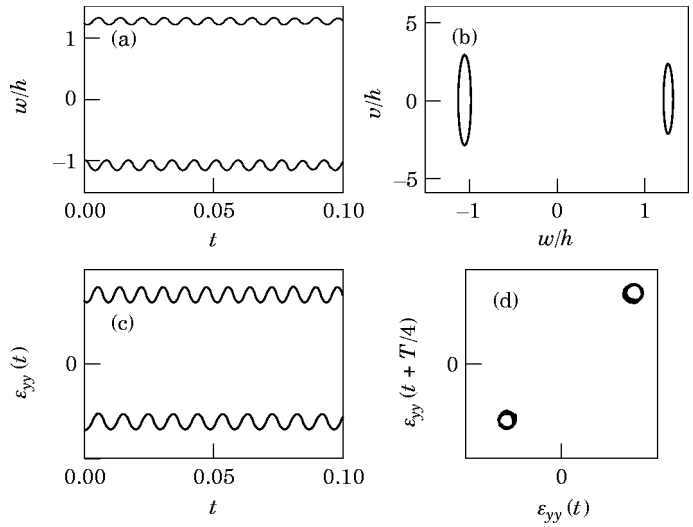

Figure 5. Coexisting small amplitude oscillations of the plate at $(\xi,\eta) = (0{\cdot}583,0{\cdot}416)$ with $\Delta T/\Delta T_{cr}^{flat} = 1{\cdot}76$, $\Delta P = 130\text{dB}$ and $\omega = 120\text{Hz}$; (a,b) numerical and (c,d) experiments.

In Figure 6 are shown the power spectra and correlation functions corresponding to the primary branch oscillation shown in Figure 2. The PSD of the displacement for the numerical case indicates that the primary response frequency is equal to the excitation frequency. There is, however, a small contribution at 245 Hz. The experiments confirm these results with slight exceptions. The strain spectrum shown in Figure 6(c) shows a distinct peak at 240 Hz, in agreement with the simulation. As before, the experiment exhibits higher peaks at the fundamental frequency and its harmonics, and a low level continuous distribution of energy throughout the frequency range.

The correlation function for the simulation shows that the response is periodic with a first zero crossing time of approximately 0·0021 s. The experimental correlation function experiences a slight decay. However, as found in the simulation, the experimental

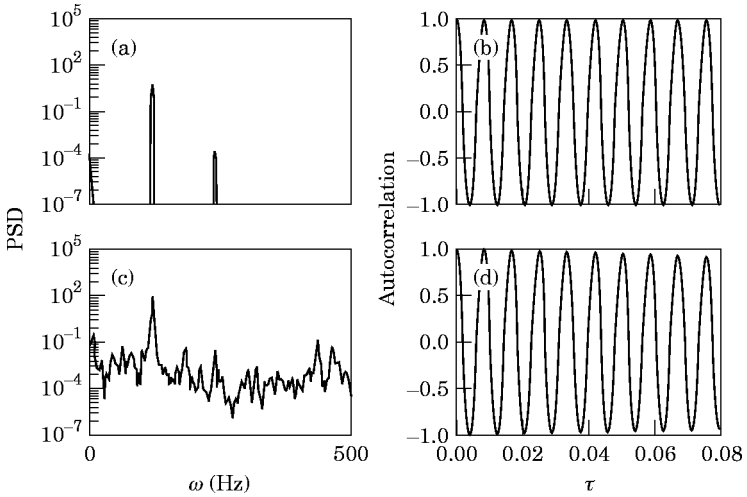

Figure 6. Numerical (a,b) and experimental (c,d) power spectra and correlation functions for the response in Figure 5.

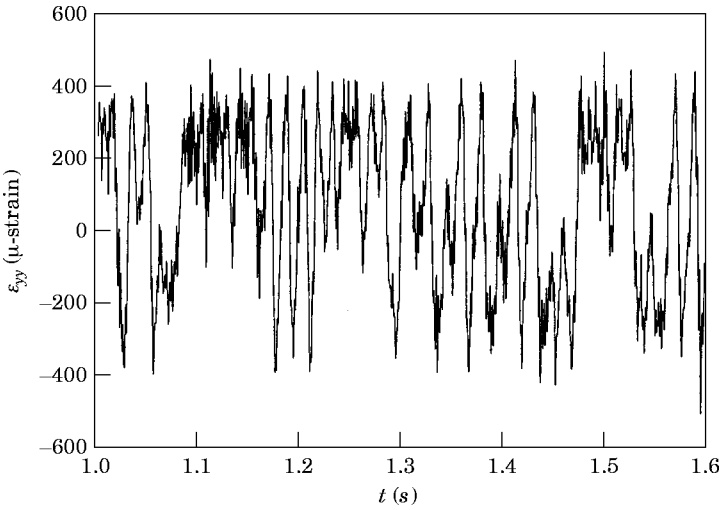

Figure 7. The experimental snap-through response of the plate at $(\xi,\eta) = (0{\cdot}583,0{\cdot}416)$ for $\Delta T/\Delta T_{cr}^{flat} = 1{\cdot}53$, $\Delta P = 155$dB and $\omega = 115$Hz.

characteristic time is almost a quarter of a forcing period and is used as the embedding lag in Figure 5(d).

6. GLOBAL BEHAVIOR

Acoustically excited snap-through motions, often a contributing factor to sonic fatigue, are global oscillations in the sense that they occur about and between multiple equilibria. Furthermore, these vibrations are often complicated and, as a result, difficult to characterize. Here, a variety of techniques is employed to quantify the temporal and, to some extent, the spatial behavior of typical snap-through oscillations. These include the time and frequency domain approaches discussed in sections 5.1 and 5.2, fractal dimensions, and Lyapunov exponents.

In the following sections a temperature ratio of $\Delta T/\Delta T_{cr}^{flat} = 1{\cdot}53$ is applied along with a harmonic acoustic excitation at a sound pressure level of 155 dB and a frequency of $\omega = 115$ Hz. The experimentally measured fundamental frequency of the primary branch was 106 Hz.

6.1. TIME AND FREQUENCY DOMAIN APPROACH

In Figure 7 is shown 0·6 s of an experimental snap-through time series. This particular test was allowed to run for over a minute before data was taken to ensure that the response was in a steady state. In the 0·6 s shown, there are numerous oscillations about and between the two stable equilibria and there is no discernible periodicity to the response.

The numerical (a) and experimental (c) time series are compared on a more appropriate time scale in Figure 8. Both show seemingly aperiodic oscillations, with a high frequency component that is not apparent in Figure 7. The accompanying pseudo-phase planes are shown for the simulation and experiment in Figures 8(b) and (d), respectively. Again, the experimental result is obtained using time delay embedding with a time lag obtained from the first crossing of the autocorrelation function. Both plots show tangled trajectories commonly associated with complex motion. However, this is not sufficient to classify the motion as chaotic. Because this system is spatially extended, the complex trajectory could

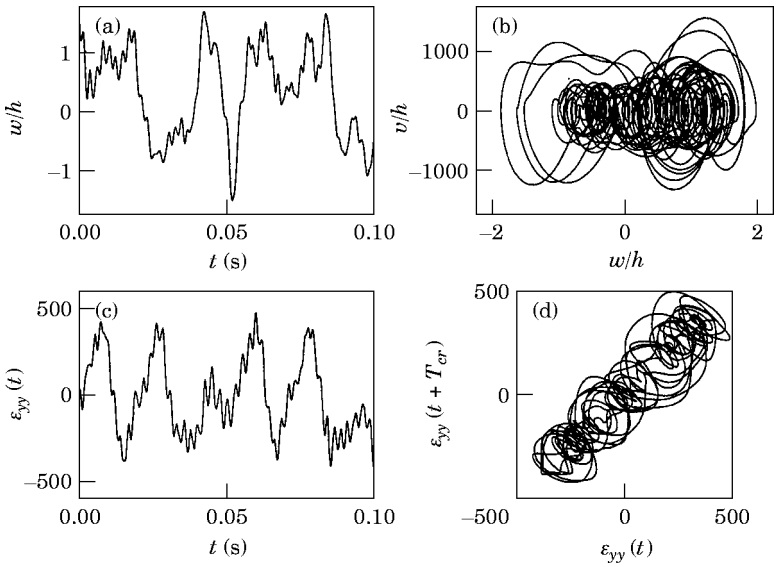

Figure 8. The snap-through response at $(\xi,\eta) = (0{\cdot}583,0{\cdot}416)$ for (a,b) simulation and (c,d) experiment.

simply result from projecting the modal contributions in N dimensions down to two dimensions.

The power spectra and autocorrelation functions for this response are shown in Figure 9. Both the simulation (a) and experiment (c) show broadband characteristics, with distinct peaks at the excitation frequency. In addition, both show similar behavior over the low and intermediate frequency range. Broad peaks appear in the high frequency range for the experimental spectra, but do not appear in the simulation. As in the periodic responses, the levels are similar in the low frequency range, but in the high frequency range the experiment contains more energy.

For both simulation (Figure 9(b)) and experiment (Figure 9(d)) there is a dramatic loss of autocorrelation, which provides some quantitative confirmation that the response is

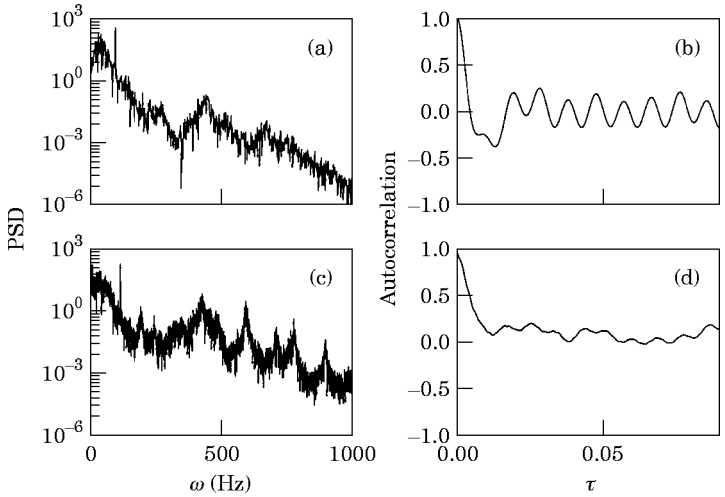

Figure 9. Numerical (a,) and experimental (c,d) power spectra and correlation functions for the time series in Figure 8.

temporally complex. The autocorrelation function also provides a measure for a characteristic time scale associated with the response via the first zero crossing. This time is also used as the embedding lag time. The first crossing for the simulation occurs at $\tau_{cr} = 0{\cdot}0038$ s. Because the experimental correlation function curves up before crossing, an appropriate measure of τ_{cr} may be obtained by extending a straight line along the initial descent of the function. The intersection of this line with the zero axis serves as the first crossing. This occurs at approximately $\tau_{cr} = 0{\cdot}0048$ s.

Considerable information regarding this typical response has been gained. In both theory and experiment, the snap-through response of the plate appears to be temporally complex which suggests that the motion may be chaotic. However, the techniques employed thus far provide only a qualitative measure for chaos and are insufficient to conclude that the motion is chaotic. Consequently, a fractal dimension and Lyapunov exponent calculation are undertaken in the following sections.

6.2. FRACTAL DIMENSION

The dimension of a set of points provides a measure for the number of co-ordinates which are necessary to describe the set. In the case of plate dynamics, the set of points under consideration is the plate's trajectory in the phase space and the dimension represents the minimum number of co-ordinates (or modal coefficients) required to represent the motion. For example, a static situation corresponds to one point in the phase space and, consequently, has dimension zero. No modes are needed to describe the motion, since there is no motion. Periodic orbits form a closed curve and thus have dimension one. Chaotic orbits, on the other hand, form a complex geometric structure (fractal) which requires a non-integer dimension to describe it. Furthermore, the dimension indicates the "size" of the subspace within the original phase space on which the attractor lies. Examples of fractal geometric structure abound, as do estimates of their dimension (see references [25–28]).

The reason for computing the fractal dimension for the snap-through response is two-fold. First, it shows that this complex motion does exist on an attractor of finite size. This is in contrast to a truly random signal, the dimension of which increases without bound. Second, it indicates the minimum number of times that the signal must be embedded to adequately recreate the phase space for the attractor. For example, a system with dimension 3·8 would require at least four successive embeddings to represent the motion. Also, knowing the minimum number of embeddings is needed to compute the Lyapunov exponents for the motion.

It should be pointed out that while a fractal dimension calculation provides a measure for the number of modes involved, it does not indicate what these modes are. In this sense, it only provides a measure for the spatial complexity of the motion but does not suggest what the attractor "looks like".

The correlation dimension is one common measure of the dimension of a response [26]. This approach takes a time series, embeds it (to a specified dimension) and computes the number of points, $C(r)$, falling within a radius r in this embedded space. The dimension then relates the behavior of $C(r)$ to r, and is defined as

$$d_c = \lim_{r \to 0} \frac{\log (C(r))}{\log (r)}. \tag{25}$$

The reason for such a definition is somewhat more evident if written

$$C(r) \propto r^{d_c}. \tag{26}$$

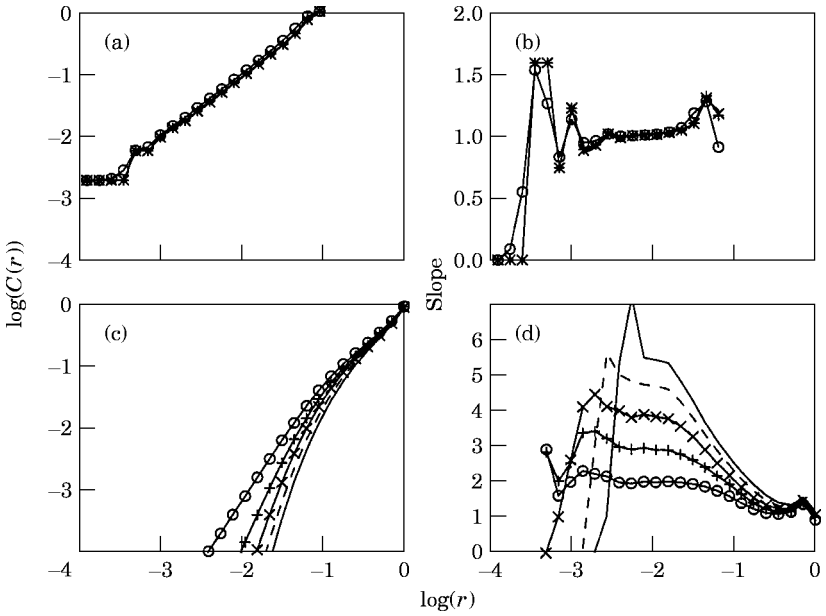

Figure 10. The fractal dimension and slopes for the periodic orbits of Figure 3; (a,b) numerical and (c,d) experimental. Various embeddings are shown: ——, 6-D; – – –, 5-D; –×–, 4-D; –+–, 3-D; –○–, 2-D.

This agrees with our previous examples. For a point ($d_c = 0$), the number of points $C(r)$ does not increase with r. For a closed orbit ($d_c = 1$), the number of points $C(r)$ increases linearly with r.

However, the dimension computed can never exceed the dimension of the reconstructed orbit (i.e., the specified embedding dimension). For example, a signal which has been embedded twice cannot render a dimension any larger than two. The common remedy to this problem is to compute the correlation dimension for a variety of different embedding dimensions. At some number of embeddings, the correlation dimension settles to a final value and is insensitive to additional embeddings.

The correlation dimension was first developed by Grassberger and Procaccia [26] and discussed further in reference [27]. The algorithm used throughout this study is described in reference [29]. There are fundamental limitations placed on the data sets used to compute the fractal dimension and, in the next section, the Lyapunov exponents. It has been shown that there are restrictions placed on the length of the time series required if meaningful results are to be obtained (see references [26, 27, 30–32]). For example, if the time series is too short, it will not encompass enough of the attractor and the resulting dimension will not be a representative value for the entire attractor. A "rule of thumb" often employed is that the minimum number of points is approximately $N \geqslant 10^d$, where d is the dimension of the attractor. The results that follow are based on 32 768 ($=2^{15}$) data points and, as such, the maximum dimension that may be obtained with any certainty is approximately 4·5.

To begin with, consider the pre-critical, linear response shown in Figure 3. The dimension of this simple closed orbit should be one. Based on equation (25), the correlation dimension is given as the local slope of this log–log plot. The local slopes may be computed for each point based on its two nearest neighbors. The numerical dimension results and slopes for the simulation are shown in Figures 10(a) and (b). As expected, the dimension levels off at $d_c = 1$ for all embedding dimensions attempted (2–6). The experimental

dimension results, shown in Figures 10(c) and (d), are quite different. From Figure 10(d), it appears that the dimension estimate changes dramatically with subsequent embeddings, and it might be tempting to conclude that either the response is random (a low signal to noise ratio) or that it has a high dimensional attractor. Clearly, this response is not random nor is it high dimensional, as evidenced by Figures 3 and 4. The poor convergence behavior is a result of having *some* noise in the signal, albeit at a low level. It has been shown that by adding low level white noise to a periodic orbit of a one-degree-of-freedom oscillator, the correlation dimension does not converge with subsequent embeddings [33]. In fact, the results in reference [33] appear very similar to those shown in Figures 10(c) and (d). This suggests that, at the very least, this particular algorithm is sensitive to the presence of even low level noise. This establishes the quality of results we may expect from both numerical and experimental data.

Figure 11(a) is a plot of $\log(C(r))$ versus $\log(r)$ for the numerical snap-through response. A variety of embedding dimensions, ranging from 2 to 6, is shown. From Figure 11(b), it is evident that the dimension saturates for the two- and three-dimensional embeddings, since there are distinct plateaus at 2 and 3, respectively, for the intermediate range of $\log(r)$. For higher-dimensional embeddings, the slopes do not level off to an obvious fixed plateau. However, the rate of change of the slopes with increased embedding dimension does decrease, suggesting that the motion lies on a low-dimensional attractor. The dimension is bounded and it can be estimated to be in the range of $3{\cdot}5 \leqslant d_c \leqslant 4{\cdot}5$.

The experimental snap-through results are shown in Figure 11(c) and the local slopes appear in Figure 11(d). Again, the dimension saturates for the two- and three-dimensional embeddings. However, the dimension increases significantly with each additional embedding and it appears that the dimension is beyond 4·5 (the maximum dimension we can compute with any confidence). To this point, all that can be said is that the dimension is not below 4·5. In fact, there is no evidence that this oscillation exists on a finite-dimensional attractor; i.e., it could be random data resulting from a poor signal to

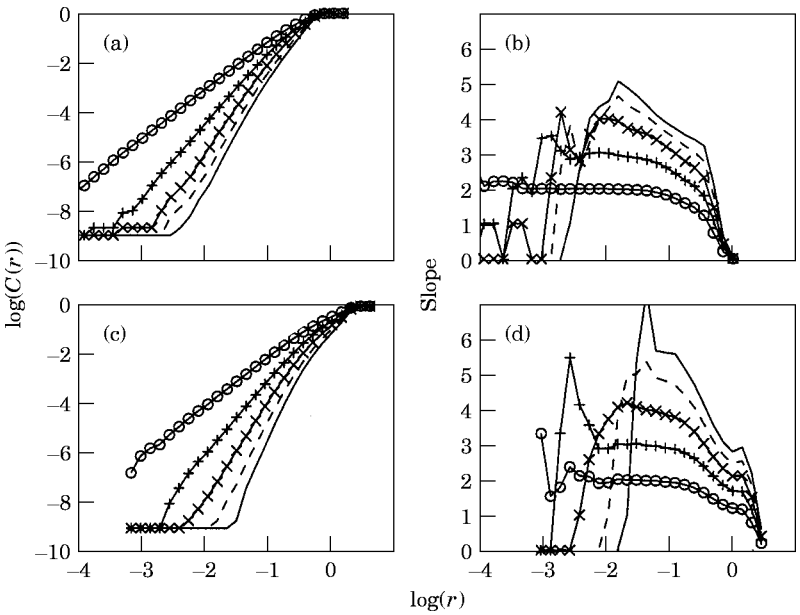

Figure 11. The fractal dimension and slopes for the snap-through oscillations of Figure 8; (a,b) numerical and (c,d) experiment. Various embeddings are shown: ——, 6-D; – – –, 5-D; –×–, 4-D; –+–, 3-D; –○–, 2-D.

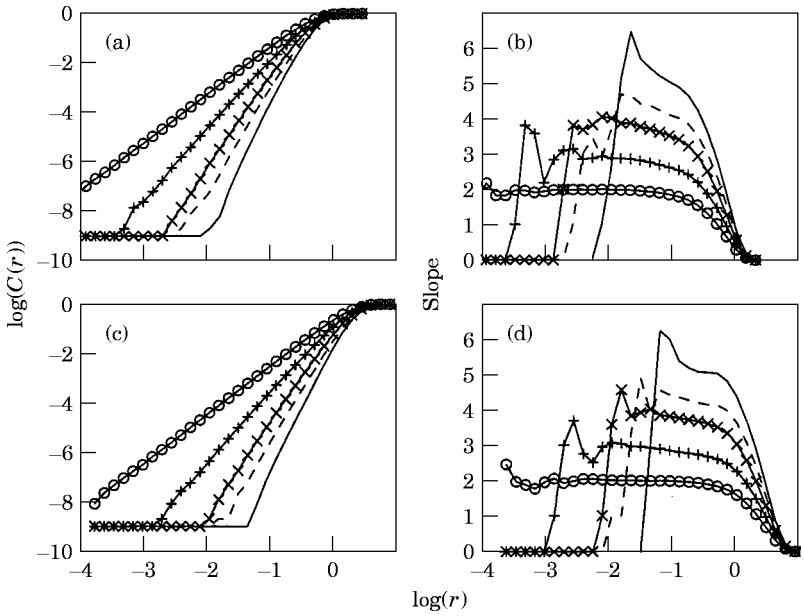

Figure 12. The fractal dimension and corresponding slopes for randomized signals; (a,b) numerical and (c,d) experimental. Various embeddings are shown: ——, 6-D; – – –, 5-D; –×–, 4-D; –+–, 3-D; –○–, 2-D.

noise ratio. This is *not* the case for this experiment since the levels, seen in Figure 7, are on the order of hundreds of micro-strain while the noise level is on the order of one. Nonetheless, the dimension estimate does not indicate this.

It has been suggested, in cases like this, that the dimension of the signal should be compared to the dimension of filtered noise [34]. If a significant difference arises, then it can be assumed that the failure of the original dimension to converge is because the signal is complex and lies on a high-dimensional attractor rather than being filtered white noise. The "random" signal may be obtained by taking the Fourier transform of the original signal, randomizing the phase and inverting the transform back to the time domain. In this way, the time series of the two signals are vastly different but their power spectra are the same (the magnitude of the FFT has not been changed).

For completeness, this procedure is carried out on both the numerical and experimental time series. The dimension results for the randomized numerical signals are shown in Figures 12(a) and (b). Comparing Figure 12(b) with Figure 11(b), there are obvious differences. Most notably, the slopes of the randomized signal continue to increase with successive embeddings, while the slopes from the original data increase much more slowly, suggesting a lower-dimensional attractor.

The dimension results for the randomized experimental signal are shown in Figures 12(c) and (d). Again, the slopes of the randomized signal continue to increase with embedding dimension and the rate of increase does not appear to be decreasing. This is consistent with the results for the dimension of the randomized numerical signal. However, in contrast to the results of numerical simulation, the slopes from the raw signal and the randomized signal do *not* differ significantly. As a result, a stronger statement about the fractal dimension of the experimental signal cannot be made. So, although the experiment is not noisy (because of the large signal to noise ratio), the dimension results are not dissimilar to random data. In effect, it must be concluded that either the experimental oscillation has a complex, high-dimensional attractor which cannot be measured from this

finite data set or the algorithm is too sensitive to low level noise to produce a satisfactory result. In either case, the dimension is not evident from this data.

The conclusion is that the dimension of the numerical response is $3{\cdot}5 \leqslant d_c \leqslant 4{\cdot}5$, while the dimension of the experimental response is still unknown. More importantly, these results underscore the need for caution in computing and interpreting dimension results obtained from experimental data.

6.3. LYAPUNOV EXPONENTS

One underlying characteristic of chaotic motion is the average exponential divergence of nearby trajectories for short times in the phase space. Because the motion remains bounded, this average divergence occurs only for short times. The separation of the two trajectories in the ith direction of the phase space is given by

$$p_i(t) = p_i(0)\, \mathrm{e}^{\lambda_i t}, \tag{27}$$

where λ_i is the ith Lyapunov exponent (L.E.). If a response has at least one positive Lyapunov exponent, trajectories diverge in the unstable direction and the motion is chaotic.

The methods for computing the Lyapunov exponents for simulation and experiment are quite different, and have been the subject of considerable research. Although a brief description of these techniques is presented here, the reader is encouraged to consult references [23] and [35–37]. Based on these works, a code was developed by the authors to compute the Lyapunov exponents for the plate from numerical simulation. The experimental Lyapunov exponents, on the other hand, were computed using the public software LCE-EXP+ [38].

In the approach used for the simulation results, the system is integrated with the full non-linear equations until a steady state response is attained. At this point, the motion is considered to be frozen at $t = t_0$. The point in the phase space occupied by the non-linear flow is termed the "fiducial" point. Nineteen initial conditions are defined along the 18 phase space directions and the time axis at a small distance $p(0)$ from the fiducial point. These initial conditions may be seen as the principal axes of a 19-dimensional sphere centered at the fiducial point. The integration is then continued using the full non-linear equations to integrate the fiducial point. Simultaneously, the principal axes are integrated using a set of equations linearized about the fiducial trajectory. As the integration proceeds, the phase space is distorted under the influence of the manifolds. Periodically, the relative stretching or compression of these axes may be computed by the formula

$$\lambda_i = \frac{1}{(t - t_0)} \ln\left(\frac{p_i(t)}{p_i(0)}\right). \tag{28}$$

One complication arises if an unstable direction exists. In this case, the linearized trajectories tend to align themselves with the unstable direction. As a result, if the integration time between L.E. calculations, $t - t_0$, is too long, the different trajectories become indistinguishable and the L.E.'s cannot be calculated. To remedy this problem, a Gram–Schmidt re-orthonormalization procedure is performed several times during the interval $t - t_0$. The entire procedure is carried out numerous times, so that the exponents may be averaged over the attractor.

In an experimental situation, the response of the system is measured in terms of a single observable quantity. In this application, the strain response at one point on the plate is used. To compute the Lyapunov exponents, the phase space is reconstructed using time delay embeddings. Unfortunately, the minimum number of embedding corresponds to the

fractal dimension and, as shown in the previous section, a reliable dimension could not be determined. Nonetheless, for the remainder of this section a five-dimensional embedding is presumed to be sufficient. However, the results of the experimental Lyapunov exponent calculation should be viewed with some skepticism.

The experimental data are embedded five times with a delay time corresponding to the first crossing of the correlation function. Next, a fiducial point is chosen and a line search (in time) is conducted through the embedded phase space to locate nearby points. Since "nearby" is a fairly subjective term, a trial and error approach was taken to determine an appropriate length scale. The length used is 25 μ-strain. In addition, there is a certain time interval, close to the fiducial point, over which points may not be used to avoid autocorrelation effects. As recommended in reference [38], this time was set equal to one forcing period. Having obtained nearby points in the phase space, the local behavior of these trajectories is monitored and the Lyapunov exponents are computed by fitting (in a least square sense) an exponential function to the separation. This procedure is carried out for a number of fiducial points so that the exponents may be averaged over the reconstructed attractor.

In Figure 13(a) all 19 numerical Lyapunov exponents are shown as functions of the total number of local exponents computed. These results show that there are positive Lyapunov exponents, which guarantees that the response is chaotic. In fact, because there are multiple

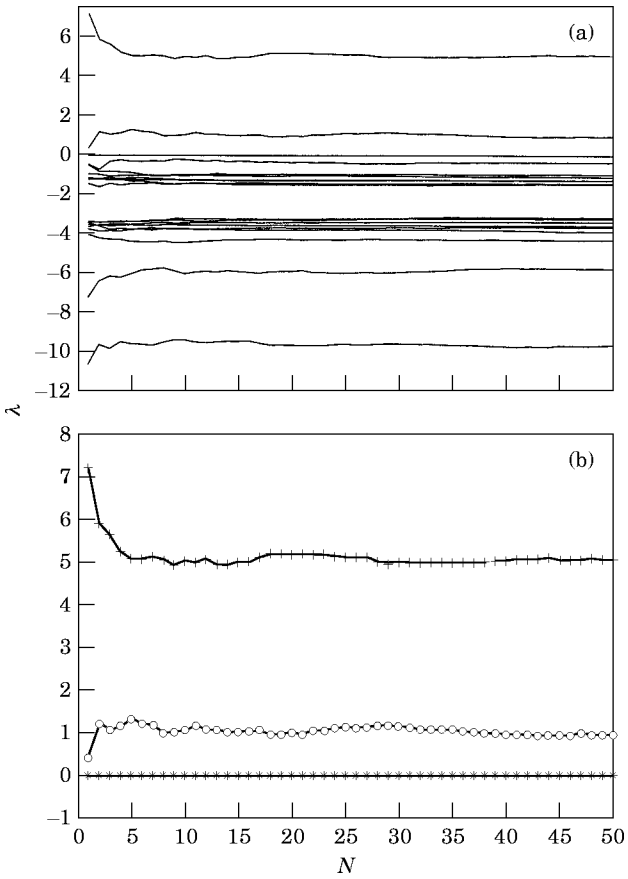

Figure 13. Numerical Lyapunov exponents for the snap-through response: (a) all 19 exponents and (b) the positive and zero exponents.

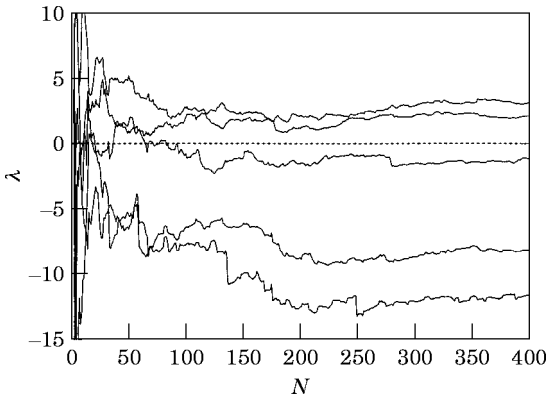

Figure 14. Experimental Lyapunov exponents computed by LCE-EXP+ using a five-dimensional embedding.

positive Lyapunov exponents, in this case *two*, this motion is an example of "hyper-chaos" [25]. The convergence behavior of these positive exponents, as they are averaged over the attractor, is more clearly demonstrated in Figure 13(b).

From these results, several important observations should be made. Although positive Lyapunov exponents assure a chaotic response, the magnitude of the exponents indicates the relative "strength" of the chaos involved. In other words, large exponents lead to more rapid exponential divergence and, hence, a faster loss of predictability. Similarly, multiple positive exponents suggest a stronger chaotic phenomenon. Based on these numerical results, the snap-through response of the plate is strongly chaotic.

From Figure 13(a) it is evident that the sum of the Lyapunov exponents is negative. This is consistent with the fact that, to preserve boundedness, volumes in the phase space must contract despite the exponential divergence in certain directions [39]. This is easily shown by considering an N-volume given by the product of the $p_i(t)$'s:

$$p_1 \cdot p_2 \cdots p_N = (p(0)^N)\, \mathrm{e}^{(\lambda_1 + \lambda_2 + \cdots + \lambda_N)}. \tag{29}$$

The expression governing the volume contraction is

$$\Lambda = \sum \lambda_i < 0.$$

Another important feature of these results is the zero Lyapunov exponent. This exponent corresponds to the principal direction along the time axis. This direction is expected to be unstretched and uncompressed under the action of the differential equations, since the right side of the time equation is uncoupled from the other state variables (i.e., $\mathrm{d}x_{19}/\mathrm{d}t = 1$). A somewhat more intuitive argument is that the evolution of time (the behavior along the time axis) is independent of the physical evolution of the motion.

In Figure 14 the Lyapunov exponents computed in LCE-EXP+ are shown for the experimental snap-through response of the plate having embedded the data five times. Several features stand out. First, there are two positive exponents, which suggests that the motion is hyperchaotic. Second, the sum of the exponents are negative, in keeping with the boundedness restriction. Finally, there is no zero exponent. This fact is anticipated, since all of the embedding dimensions behave like a physical dimension of the attractor rather than the time dimension.

From these results, the numerical time responses may be properly classified as hyperchaotic based on the multiple positive Lyapunov exponents. Less can be said with

certainty about the experimental time series. Although it also has two positive exponents, suggesting hyperchaos, there is no evidence that the data were embedded a sufficient number of times. The only reasonable conclusion is that it *appears* to be hyperchaotic.

7. CONCLUSIONS

Theoretical and experimental results were presented to characterize the dynamic response of homogeneous, fully clamped, rectangular plates under narrow-band acoustic excitation and uniform thermal loads. Small amplitude oscillations about the pre- and post-critical regimes were shown to be linear using time series, pseudo-phase planes, power spectra and autocorrelation functions. Considerable agreement between simulation and experiment was evident.

In both simulation and experiment, the snap-through response appeared to be aperiodic with broadband power spectra and a dramatic loss of correlation. However, differences arose in the fractal dimension calculation.

While dimension estimates for the numerical snap-through response (Figure 11(b)) did not yield a fixed dimension (plateau), they do appear changing more slowly with successive embedding and, hence, are converging in the vicinity of $3{\cdot}5 \leqslant d_c \leqslant 4{\cdot}5$. These results are supported by the fact that the slopes increased without bound for the randomized numerical data (Figure 12(b)). This contrasts with the dimension estimates for the numerical periodic signal (Figure 10(b)), which clearly converged to a value of $d_c = 1$.

The experimental dimension is a more complicated situation. The dimension (Figure 11(d)) does not appear to converge and, in fact, is virtually indistinguishable from the randomized signal (Figure 12(d)). However, the original signal is the result of purely deterministic (non-random) inputs and there is a high signal to noise ratio. It is believed that the low level background noise is responsible for corrupting the dimension estimate. This is also demonstrated by the dimension estimate for the small amplitude experimental periodic signal (Figure 10(c)) where, again, the results do not converge.

The Lyapunov exponent calculation confirms that the snap-through simulation has two positive exponents and, as such, is an example of higher-dimensional chaos. In other words, it is hyperchaotic. Less confidence may be placed in the experimental Lyapunov exponents since the embedding dimension is in question. However, based on a five-dimensional reconstructed phase space (embedded), the experimental snap-through motion also *appears* to be hyperchaotic.

ACKNOWLEDGMENT

The authors gratefully acknowledge the support of the Structural Acoustics Branch of the NASA Langley Research Center under NASA GSRP grant number NGT-50989.

REFERENCES

1. J. F. Mixon and L. Roussos 1987 *NASA Technical Memorandum* 89143. Acoustic fatigue: overview of activities at NASA Langley.
2. B. L. Clarkson 1994 *NASA Contract Report* 4587. Review of sonic fatigue technology.

3. E. H. Dowell 1966 *American Institute of Aeronautics and Astronautics Journal* **4**, 1267–1275. Nonlinear oscillations of a fluttering plate.
4. E. H. Dowell 1985 *Journal of Sound and Vibration* **85**, 195–204. Flutter of a buckled plate as an example of chaotic motion of a deterministic autonomous system.
5. C. F. Ng 1989 *Journal of Aircraft* **26**, 281–288. Nonlinear and snap-through responses of curved panels to intense acoustic excitation.
6. C. F. Ng and S. A. Clevenson 1989 *Journal of Aircraft* **28**, 275–281. High-Intensity acoustic tests of a thermally stressed plate.
7. W. T. Tseng and J. Dugundji 1971 *Journal of Applied Mechanics* **38**, 467–476. Nonlinear vibrations of a buckled beam under harmonic excitation.
8. T. Penketgorn, K. B. Rojiani and R. H. Plaut 1989 *Probabilistic Engineering Mechanics* **4**, 114–119. Snap-through of a shallow arch under random loading.
9. S. A. Clevenson and E. F. Daniels 1992 *NASA Technical Memorandum* 104106. Capabilities of the thermal acoustic fatigue apparatus.
10. K. D. Murphy, L. N. Virgin and S. A. Rizzi 1996 Submitted to *Journal of Vibration and Acoustics*. The effect of thermal prestress on the free vibration characteristics of clamped, rectangular plates: theory and experiment.
11. E. H. Dowell 1975 *Aeroelasticity of Plates and Shells*. Leyden: Noordhoff International.
12. A. S. Volmir 1967 *Air Force Flight Dynamics Laboratory*, *Wright–Patterson Air Force Base*, *Ohio* AFFDL-TR-66-216. Flexible plates and shells.
13. C. Y. Chia 1980 *Nonlinear Analysis of Plates*. New York: McGraw-Hill.
14. C. S. Ventres and E. H. Dowell 1970 *American Institute of Aeronautics and Astronautics Journal* **8**, 2022–2030. Comparison of theory and experiment for nonlinear flutter of loaded plates.
15. R. V. Southwell 1932 *Proceedings of the Royal Society of London* **135A**, 601–616. On the analysis of experimental observations in problems of elastic stability.
16. L. Mierovitch 1986 *Elements of Vibration Analysis*. New York: McGraw-Hill.
17. J. L. Humar 1990 *Dynamics of Structures*. Englewood Cliffs, NJ: Prentice-Hall.
18. L. E. Kinsler, A. R. Frey, A. B. Coppens and J. V. Sanders 1982 *Fundamentals of Acoustics*. New York: John Wiley.
19. A. C. Hindmarsh 1983 in *Scientific Computing* (R. S. Stepleman editor), 55–64. Odepack, a systematized collection of ODE solvers.
20. W. H. Press, B. P. Flannery, S. A. Teukolsky and W. T. Vetterling 1989 *Numerical Recipes*. New York: Cambridge University Press.
21. C. F. Gerald and P. O. Wheatley 1989 *Applied Numerical Analysis*. New York: Addison-Wesley.
22. D. S. Broomhead and G. P. King 1986 *Physica D* **20**, 217–236. Extracting qualitative dynamics from a time series.
23. H. D. I. Abarbanel 1993 *Reviews of Modern Physics* **65**, 1331–1390. The analysis of observed chaotic data in physical systems.
24. D. E. Newland 1984 *An Introduction to Random Vibrations and Spectral Analysis*. New York: Longman.
25. F. C. Moon 1992 *Chaotic and Fractal Dynamics*. New York: John Wiley.
26. P. Grassberger and I. Procaccia 1983 *Physical Review Letters* **50**, 346–349. Characterization of strange attractors.
27. J. Theiler 1987 *Physical Review A* **36**, 4456–4462. Efficient algorithm for estimating the correlation dimension from a set of data points.
28. J. D. Farmer, E. Ott and J. A. Yorke 1983 *Physica D* **7**, 153–180. The dimension of chaotic attractors.
29. J. Goldberg 1993 *Software Documentation* 1–4. Using the Correlation Dimension Code: Grass.
30. J. Theiler 1986 *Physical Review A* **34**, 2427–2432. Spurious dimension from correlation algorithms applied to limited time-series data.
31. J. P. Eckmann and D. Ruelle 1992 *Physica D* **56**, 185–187. Fundamental limitations for estimating dimensions and Lyapunov exponents in dynamical systems.
32. N. B. Abraham, A. M. Albano, B. Das, G. De Guzman, S. Young, R. S. Gioggia, G. P. Puccioni and J. R. Tredicce 1986 *Physics Letters A* **114**, 217–221. Calculating the dimension of attractors from small data sets.
33. P. V. Bayly 1993 *Ph.D. Thesis*, *Duke University*. Measurements of instability and disorder in nonlinear mechanical and cardiac oscillations.
34. J. Theiler 1990 *Optical Society of America* **7**, 1055–1073. Estimating fractal dimension.

35. A. Wolf, J. B. Swift, H. L. Swinner and J. A. Vastano 1985 *Physica D* **16**, 285–317. Determining Lyapunov exponents from a time series.
36. T. S. Parker and L. O. Chua 1989 *Practical Numerical Algorithms for Chaotic Systems*. New York: Springer-Verlag.
37. P. G. Grassberger, T. Schreiber and C. Schaffrath 1991 *International Journal of Bifurcations and Chaos* **1**, 521–547. Nonlinear time sequence analysis.
38. T. M. Kruel and M. Eiswirth 1991 *Software Documentation* 1–19. LCE-EXP: a program for the calculation of the complete spectrum of Lyapunov exponents from a time-series of experimental data.
39. J. M. T. Thompson and H. B. Stewart 1986 *Nonlinear Dynamics and Chaos*. Chichester: John Wiley.